JOURNAL OF GEOPHYSICAL RESEARCH, VOL. 115, D00H25, doi:10.1029/2009JD012376, 2010

Validation of the CALIPSO-CALIOP extinction coefficients from in situ observations in midlatitude cirrus clouds during the CIRCLE-2 experiment

Guillaume Mioche,[1] Damien Josset,[2] Jean-François Gayet,[1] Jacques Pelon,[2] Anne Garnier,[2] Andreas Minikin,[3] and Alfons Schwarzenboeck[1]

Received 30 April 2009; revised 11 December 2009; accepted 11 January 2010; published 26 June 2010.

[1] This paper presents a comparison of combined Cloud-Aerosol Lidar and Infrared Pathfinder Satellite Observation (CALIPSO) and Cloud-Aerosol Lidar with Orthogonal Polarization (CALIOP) extinction retrievals with airborne lidar and in situ cirrus cloud measurements. Specially oriented research flights were carried out in western Europe in May 2007 during the Cirrus Cloud Experiment (CIRCLE-2) with the German Deutsches Zentrum für Luft- und Raumfahrt (DLR) and the French Service des Avions Français Instrumentés pour la Recherche en Environnement (SAFIRE) Falcon aircraft equipped for remote and in situ measurements, respectively. Four cirrus cloud situations including thin cirrus layers and outflow cirrus linked to midlatitude fronts and convective systems were chosen to perform experimental collocated observations along the satellite overpasses. The measurements were carried out with temperatures ranging between −38°C and −60°C and with extinction coefficients no larger than 2 km^{-1}. Comparisons between CALIOP and airborne lidar (LEANDRE New Generation (LNG)) attenuated backscatter coefficients reveal much larger CALIOP values for one frontal cirrus situation which could be explained by oriented pristine ice crystals. During the four selected cases the CALIOP cirrus extinction profiles were compared with in situ extinction coefficients derived from the Polar Nephelometer. The results show a very good agreement for two situations (frontal and outflow cases) despite very different cloud conditions. The slope parameters of linear fittings of CALIOP extinction coefficients with respect to in situ measurements are 0.90 and 0.94, with correlation coefficients of 0.69 and only 0.36 for the latter case because of a small number of measurements. On the contrary, significant differences are evidenced for two other situations. In thin frontal cirrus at temperatures ranging between −58°C and −60°C, systematic larger CALIOP extinctions can be explained by horizontally oriented ice crystals with prevalent planar-plate shape as revealed by the Cloud Particle Imager instrument. This nicely explains the disagreements between CALIOP and LNG observations for that case. For the last cirrus situation related to dense outflow cirrus, CALIOP extinctions are systematically lower than the in situ observations. No clear explanations can be drawn to assess this feature, but the shattering of ice crystals on probe tips may enhance the measured extinction because numerous large ice crystals are observed during this cirrus situation. Finally, relationships between the ice water content and the extinction coefficient, the effective diameter, and the temperature are determined from this in situ measurements data set.

Citation: Mioche, G., D. Josset, J.-F. Gayet, J. Pelon, A. Garnier, A. Minikin, and A. Schwarzenboeck (2010), Validation of the CALIPSO-CALIOP extinction coefficients from in situ observations in midlatitude cirrus clouds during the CIRCLE-2 experiment, *J. Geophys. Res.*, *115*, D00H25, doi:10.1029/2009JD012376.

[1]Laboratoire de Météorologie Physique, UMR 6016, Université Blaise Pascal, CNRS, Aubière, France.
[2]Laboratoire Atmosphères, Milieux, Observations Spatiales, UMR 8190, Université Pierre et Marie Curie, CNRS, Paris, France.
[3]Institut für Physik der Atmosphäre, Deutsches Zentrum für Luft- und Raumfahrt, Wessling, Germany.

0148-0227/10/2009JD012376

1. Introduction

[2] With a global cover of 30% of the Earth's surface [*Wylie et al.*, 1994], and because of the importance of their interaction with solar and terrestrial radiation, it is well known that cirrus clouds play a crucial role in the radiation balance of the Earth [*Liou*, 1986; *Liou and Takano*, 1994]. Their representation in global and regional climate models

needs to be as reliable as possible. Nevertheless, this remains quite difficult on a global scale due to the wide variety and distribution of cirrus types and the poor knowledge of their different microphysical and optical properties.

[3] Spaceborne observations from satellites flying together with complementary instruments, namely the A-Train, offer now new opportunities to provide an unprecedented survey of cloud properties on a global scale [*Stephens et al.*, 2002] and to assess more reliable representations of clouds to constrain global climate models. Among these satellites, the NASA/CNES Cloud-Aerosol Lidar and Infrared Pathfinder Satellite Observation (CALIPSO), launched in April 2006, is dedicated to the study of thin clouds and aerosols [*Winker et al.*, 2003, 2009]. The payload includes the Cloud-Aerosol Lidar with Orthogonal Polarization (CALIOP), which delivers for the first time, on a global-scale, multiyear, high-quality measurements of vertical profiles of aerosol and cloud backscattering properties. Lidar retrieval techniques to derive pertinent cloud and optical parameters, including the extinction coefficient, require validation strategies combining coincident measurements. Airborne campaigns with in situ and remote instruments are one strategy to obtain these measurements. For example, *Hlavka et al.* [2005] made comparisons of Geoscience Laser Altimeter System (GLAS) measurements with extinction retrievals directly determined from coincident airborne lidar measurements. Inherent to this strategy are the difficulties in collocating different measurements separated in time and space (the aircraft and satellite ground trace speeds are 200 m s^{-1} and 7 km s^{-1}, respectively). Therefore flight plans are designed to accurately follow the CALIPSO satellite track when cirrus clouds are forecasted.

[4] The coordinated German-French Cirrus Cloud Experiment (CIRCLE-2) [*Eichler et al.*, 2009], which took place in western Europe in May 2007, was devoted to a better understanding of the processes involved in cirrus cloud life cycles and to the validation of satellite observations. This airborne field campaign focused on an extensive characterization of optical and radiative properties of cirrus for improving cloud parameterizations in mesoscale and global models. Several flights were coordinated with CALIPSO overpasses for the validation of the CALIOP standard data products.

[5] The main objective of this paper is to compare the CALIPSO level 1 and level 2 products (version 2.01) with airborne lidar and in situ observations of cirrus clouds during CIRCLE-2. The interpretation of the results assesses the reliability of the algorithms that derive secondary products from CALIOP and identifies potential problems inherent to these retrieval techniques. Thanks to the in situ measurements, a secondary objective is to provide parameterizations for retrieving cirrus clouds properties (ice water content, effective diameter) from CALIOP extinction coefficient.

[6] After a brief introduction presenting the measurement strategy and the cirrus cases sampled during the campaign, the in situ instruments used to determine in situ microphysical properties of cirrus clouds and the airborne lidar are presented, as are the data analyses and the expected accuracies on retrieved parameters. The method to retrieve the extinction coefficient from CALIOP lidar is briefly reviewed. CALIOP products are compared to both the airborne lidar observations and the in situ extinction measurements. The results are discussed with the interpretation of the measurements. Finally, relationships between the ice water content and the extinction coefficient, the effective diameter, and the temperature are determined from this in situ measurements data set.

2. Field Campaign and Measurement Strategy

2.1. CIRCLE-2 Experiment

[7] The CIRCLE-2 campaign, held from 4 to 26 May 2007, involved two Falcon (F20) aircraft. The first one, operated by Deutsches Zentrum für Luft- und Raumfahrt (DLR), was equipped with microphysical and optical in situ probes. The DLR Water Vapor Lidar Experiment in Space (WALES) Lidar and a Spectral Modular Airborne Radiation measurement system (SMART) [*Wendisch et al.*, 2001] were also installed on board the DLR F20 but the data will not be considered in this study. The second Falcon, from Service des Avions Français Instrumentés pour la Recherche en Environnement (SAFIRE), was carrying remote sensing down-looking systems. The two aircraft were operated from Oberpfaffenhofen (near Munich, Germany) and Creil (near Paris, France). Both aircraft had identical performances (cruise speed of ~200 m s^{-1}, or about 9 min flight duration per degree in latitude).

[8] During the campaign, 10 flights were performed in cirrus clouds by the DLR F20 over western Europe [*Eichler et al.*, 2009]. Among them, four flights were devoted to the CALIPSO and CALIOP validation (see Table 1). We now describe the strategy of collocating airborne measurements with the satellite overpass, in order to perform comparisons as reliably as possible.

2.2. Satellite and Aircraft Collocalization Strategy

[9] The two Falcon aircraft were coordinated to fly under CALIPSO track according to the cirrus cloud forecasts over western Europe by DLR. On both aircraft, the altitude and position parameters were measured by the airborne GPS systems with an accuracy of 20 m. This allowed us to very accurately follow the satellite track for reliable comparisons and to get an accurate altitude reference for all observations.

[10] The DLR F20 flight plan consisted of several in-cloud sequences at constant levels, first near the cloud top, and then at different lower levels depending on the cloud width. Each sequence lasted about 15–20 min (or 180–250 km long) with a U-turn maneuver at the end of the sequence. The SAFIRE F20 flight strategy was to fly above the cirrus layer at the maximum ceiling (~13 000 m) with nadir looking observations.

[11] Four cirrus cloud situations were favorable for performing flights collocated in time and space along the CALIPSO overpasses. Table 1 summarizes these situations, with indications of the satellite overpass times and cloud types. On 16 and 25 May, thin frontal cirrus were observed over the Atlantic Ocean near the west coast of France, whereas on 23 and 26 May, outflow cirrus from cumulonimbus systems were measured along the northern part of Spain and over Germany. Figure 1 displays the corresponding cloud fields as observed by Moderate Resolution Imaging Spectroradiometer (MODIS) instrument on board the Aqua platform, heading the A-Train. The CALIPSO track is

Table 1. Flight Sequences Used for the CALIOP Validation During CIRCLE-2[a]

Day (in 2007)	CALIPSO Overpass Time (UTC)	Cirrus Cloud Type	DLR F20 Observations			Coordination of the Two Falcon Aircraft
			Δt (min)	Altitude (km)	Temperature (°C)	
16 May	1333	Frontal thin cirrus over ocean, West of France	−18/+12	11.9	−59	Yes
			+13/+35	11.3	−56	Yes
23 May	1318	Outflow cirrus over North of Spain	−6/+9	10.7	−52	No
			+12/+25	10.5	−50	No
25 May	1326	Frontal thin cirrus over ocean, West of France	−6/+5	10.9	−54	Yes
			+6/+14	10.6	−52	Yes
			+20/+38	10.3	−50	Yes
26 May	1232	Outflow cirrus over Germany	−8/+0	9.4 to 10	−44 to −49	LNG not working
			+1/+8	8.6 to 9.2	−38 to −44	LNG not working

[a]For each sequence, the cirrus cloud type, time lags (Δt) between the satellite overpass and the in situ observations, flight altitudes, and corresponding temperatures are given. CALIOP, Cloud-Aerosol Lidar with Orthogonal Polarization; CALIPSO, Cloud-Aerosol Lidar and Infrared Pathfinder Satellite Observation; DLR, Deutsches Zentrum für Luft- und Raumfahrt; LNG, LEANDRE New Generation.

superimposed on the composite images obtained from Dundee station. The thick lines in Figure 1 represent the approximate locations of the aircraft operations. The 16 and 25 May flights allowed direct comparisons between all observations over ocean, as the SAFIRE F20 was successfully coordinated with the DLR F20.

[12] The different cloud sequences and corresponding altitudes and temperatures are indicated in Table 1, along with the maximum time lags (Δt) between the satellite overpass and the in situ observations of the cloud sequence. Most of the time, the satellite coincidences occurred during the first sequence of the day when the DLR F20 was at its highest flight level. A time difference of about ±20 min was generally chosen between in situ measurements and the satellite overpass, consistent with the procedures used in previous validation studies [*McGill et al.*, 2007; *Barker et al.*, 2008]. However, in order to complete the observations at additional cirrus levels, two sequences with Δt extended to about 40 min were selected for frontal cirrus situations (16 and 25 May; see Table 1) because of their rather slow evolution. On the contrary, for the 26 May outflow cirrus characterized by a rapid change of the cloud structure [*Protat et al.*, 2009], the time window was reduced to a Δt of ±8 min (see Table 1). We therefore assume in the following that the natural time variability of the cirrus cloud properties is of the same order as the measured horizontal variability. During the four cirrus situations, nine cloud sequences have been selected which represent about 130 min of quasi-collocated observations.

3. Instrumentation and Data Analysis

[13] In situ measurements of microphysical and optical properties performed on board the DLR F20 were derived from two Particle Measurements System (PMS) instruments, including a Forward Scattering Spectrometer Probe FSSP-300 and a 2D-C probe, a Cloud Particle Imager (CPI) from SPEC, Incorporated, and a Polar Nephelometer probe designed at LaMP [*Gayet et al.*, 1997]. Remote sensing measurements on board the SAFIRE F20 aircraft were from the Institut Pierre Simon Laplace (IPSL) radar-lidar system [*Protat et al.*, 2004]. Only the LEANDRE New Generation (LNG) lidar [*Pelon et al.*, 1990] data are used here.

3.1. In Situ Instrumentation on Board the DLR F20

[14] Three independent techniques are used in this study: (1) the PMS FSSP-300 operated by the DLR, (2) the CPI, and (3) the Polar Nephelometer probes, operated by the Laboratoire de Météorologie Physique (LaMP). The combination of these three techniques provides a description of particles within a diameter range varying from a few micrometers (typically 3 μm) to about 2 mm. The method of data processing, the reliability of the instruments, and the uncertainties of the derived microphysical and optical

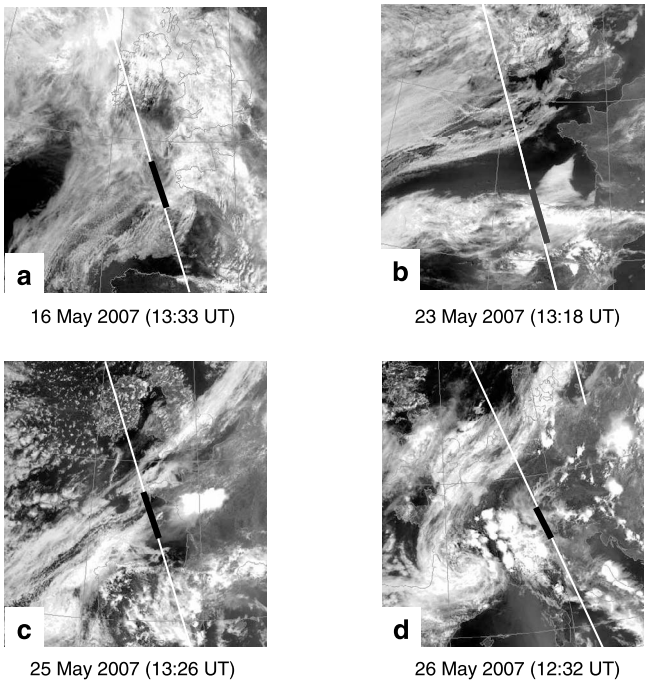

Figure 1. Cloud fields as observed by Moderate Resolution Imaging Spectroradiometer (MODIS) instrument onboard AQUA platform, showing the (a) 16, (b) 13, (c) 25, and (d) 26 May situations. The Cloud-Aerosol Lidar and Infrared Pathfinder Satellite Observation (CALIPSO) tracks are superimposed on the composite images with the Falcon flight track represented by thick lines.

parameters have been described in detail by *Gayet et al.* [2006, 2009]. For completeness, we also report interstitial aerosol data as obtained from the PMS PCASP-100X aerosol spectrometer probe, which has condensation particle counters with heated (250°C) and unheated inlets. Relative humidity was derived from measurements using a CR-2 frost point hygrometer.

[15] In the present study, particles larger than 3 μm diameter were measured by the PMS FSSP-300 optical particle counter [*Baumgardner et al.*, 1992]. For analysis of the data, the particles are assumed to be ice crystals. The upper size limit of the FSSP-300 in this study is 21.8 μm, which leads to better agreement with the first channels of the CPI and 2D-C probes in terms of particle concentration, extinction, and ice water content. The bulk quantities were calculated assuming spherical particles with a density of 0.9 g cm^{-3}.

[16] The CPI registers cloud particle images on a solid-state, one million pixel digital charge-coupled device (CCD) camera by freezing the motion of the particle using a 40 ns pulsed, high-power laser diode [*Lawson et al.*, 2001]. A particle detection system (PDS) with upstream lasers precisely defines the focal plane so that at least one particle in the image is in the focus. Each pixel in the CCD camera array has an equivalent size in the sample area of 2.3 μm, so particles of sizes from approximately 10 μm to 2 mm are imaged. The CPI images were processed using the software [*Lefèvre*, 2007] developed at LaMP, on the basis of the features and algorithms outlined in original CPIview software manual [see *Stratton Park Engineering Company*, 2005; *Lawson et al.*, 2001; *Baker and Lawson*, 2006], but providing additional information on the ice particle morphology. The software also uses the method proposed by *Lawson and Baker* [2006] for the determination of ice water content from a two-dimensional particle imagery.

[17] The Polar Nephelometer [*Gayet et al.*, 1997] measures the scattering phase function of an ensemble of cloud particles (i.e., water droplets or ice crystals or a mixture of these particles ranging from a few micrometers to about 1 mm diameter), which intersect a collimated laser beam near the focal point of a parabolic mirror. The light source is a high-power (1.0 W) multimode laser diode operating at λ = 804 nm. The data acquisition system of the airborne version of the Polar Nephelometer is designed to provide a continuous sampling volume by integrating the measured signals of each of the detectors over a selected period. For instance, the sampling volume (v) is determined by the sampling surface (10 mm long and 5 mm diameter beam) multiplied by the Falcon cruise speed of approximately 200 m s^{-1}, i.e., 1 L for an acquisition frequency of 10 Hz. This means that the detection threshold is close to one particle per liter at this frequency. Direct measurement of the scattering phase function allows particle types (water droplets or ice crystals) to be distinguished and calculation of the optical parameters to be performed, i.e., extinction coefficient and asymmetry parameter with accuracies evaluated to 25 and 4%, respectively [*Gayet et al.*, 2002a].

3.2. Lidar Remote Sensing on Board the French F20

[18] LNG is a backscatter lidar which operates at three wavelengths (355, 532, and 1064 nm), the last two being the same as those emitted by CALIOP. The LNG view angle is 3° with respect to the vertical. Therefore, a small correction in height is needed with respect to GPS altitude to position correctly the surface echo. As wide emission and reception angular fields of view (5 and 7 mrad at 1064 and 532 nm, respectively) are used, the multiple-scattering contribution is larger than usual for an airborne lidar system [*Bissonnette*, 1996].

3.3. Cloud Parameter Retrievals

3.3.1. CALIOP Operational Products

[19] The CALIOP lidar uses a laser operating at 532 and 1064 nm, with parallel and orthogonal polarization detectors at 532 nm [*Winker et al.*, 2003; *Hunt et al.*, 2009]. As described by *Vaughan et al.* [2004], the technique for deriving extinction coefficient profiles from CALIOP raw data is in three steps. The processing begins with the Selective Iterated Boundary Locator (SIBYL) to detect feature locations in the CALIOP measurements. Then the Scene Classifier Algorithm (SCA) classifies the features detected as clouds or aerosols and selects appropriate multiple-scattering factors and lidar ratios to use in the next step of processing. Finally, the Hybrid Extinction Retrieval Algorithm (HERA) retrieves the extinction coefficient profiles and optical depth of the features detected. The CALIPSO HERA is a collection of several routines that calculates extinction coefficients from a linear iterative-convergent technique. As described by *Young and Vaughan* [2009] and in part 4 of the CALIOP Algorithm Theoretical Basis Document (ATBD): Extinction Retrieval Algorithms, cloud optical properties are determined according to the following equations:

[20] The backscattered signal $P(r)$ detected from the lidar is

$$P(r) = \frac{1}{r^2} E_0 \xi [\beta_M(r) + \beta_P(r)] T_M^2(0,r) T_{O_3}^2(0,r) T_P^2(0,r) \qquad (1)$$

where ξ is the lidar system parameter (product of amplifier gain and lidar calibration factor) and E_0 is the average laser energy for a single shot or composite profile. $\beta_M(r)$ and $\beta_P(r)$ refer to the molecular volume backscatter coefficient and the particulate volume backscatter coefficient, respectively. $T_M^2(0, r)$, $T_{O_3}^2(0, r)$, and $T_P^2(0, r)$ are the molecular, ozone, and particulate two-way transmittance, respectively, between the lidar and range r. For detailed descriptions of these parameters, one can refer to the ATBD.

[21] The attenuated backscatter coefficient (ABC) is defined as

$$ABC(r) = [\beta_M(r) + \beta_P(r)] T_M^2(0,r) T_{O_3}^2(0,r) T_P^2(0,r). \qquad (2)$$

It is obtained after normalization of the lidar signal in a clear air region. For CALIOP, this region is taken between 30 and 34 km. The particulate two-way transmittance can be written as

$$T_P^2(0,r) = \exp[-2\eta(r)\tau_P(0,r)] \qquad (3)$$

where $\eta(r)$ is the multiple-scattering factor as identified from *Platt* [1979]. The particulate optical thickness τ_P is

$$\tau_P(0,r) = \int_0^r \sigma_P(r')dr' = S_P \int_0^r \beta_P(r')dr' \qquad (4)$$

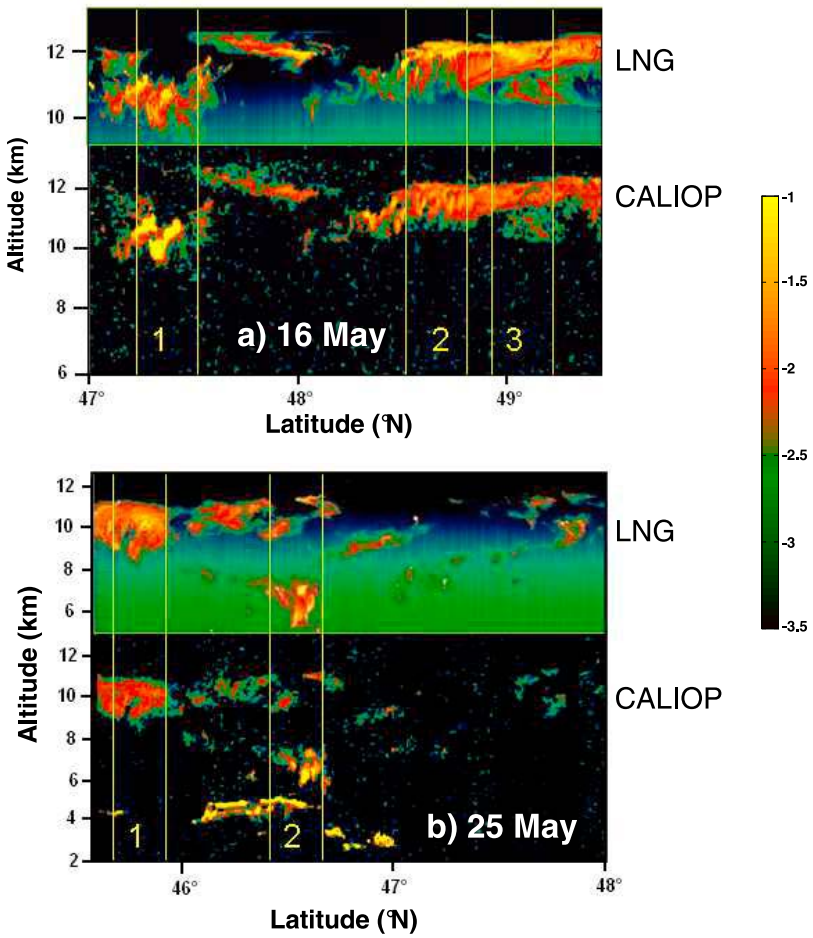

Figure 2. Latitude-height plots of the attenuated backscatter coefficient at 1064 nm as observed by Cloud-Aerosol Lidar with Orthogonal Polarization (CALIOP) on (a) 16 May (between 47°N and 49.3°N) and (b) 25 May (between 45.7°N and 48°N). The corresponding LEANDRE New Generation (LNG) vertical profiles of the attenuated backscatter coefficient at 1064 nm is superimposed to the CALIOP observations. The domains identified by rectangles are regions of interest for comparisons of backscattering properties (see Figure 3).

Finally, from equation (4), the particulate volume extinction coefficient σ_P can be written as

$$\sigma_P(r) = S_P \beta_P(r) \tag{5}$$

with S_P being the particulate extinction-to-backscatter ratio, or lidar ratio [*Sassen and Comstock*, 2001]. To solve these equations, the CALIPSO algorithms use ancillary information from meteorological analyses by NASA's Global Modeling and Assimilation Office (GMAO GEOS5) to determine the molecular number density and ozone absorption coefficient profiles and from SCA processing to determine the particulate lidar ratio and multiple-scattering factor. For the four cirrus cases discussed in this paper, the lidar ratio and the multiple-scattering factor were 25 sr and 0.6, respectively (from Cloud Layer Product data).

3.3.2. LNG Airborne Lidar

[22] Processing of the airborne lidar data is similar to CALIOP data analysis. Normalization to molecular backscattering of the lidar signal is performed just at high altitude to derive the attenuated backscatter coefficient. The required density profiles are obtained from the aircraft in situ measurements. At this period of time, the aerosol content at altitudes between 12 and 13 km remained low, leading to extinction coefficient smaller than 1.10^{-3} km^{-1} at 750 nm [*Bourassa et al.*, 2007]. Assuming an average lidar ratio (S_p) for such stratospheric particles of about 60 sr [*Chazette et al.*, 1995] leads to an induced error smaller than 10% at 532 nm. This technique could be applied in clear air regions of the observations of 16 and 25 May between 12 and 13 km (evidenced at 1064 nm as black areas in Figure 2). The normalization factor was then used over the whole leg after normalization to the energy variation. Because of uncertainties and bias in the energy measurements during the campaign, the final normalization uncertainty is expected to be on the order of 20%.

3.3.3. In Situ Observations

[23] The microphysical parameters were derived from in situ measurements by adding the contributions of the PMS FSSP-300 and the CPI. The parameter definitions are the following: (1) ice particle concentration (Conc), (2) extinction coefficient (Ext), (3) ice water content (IWC), and

(4) effective diameter (D_{eff}). This last quantity was calculated, as in earlier studies [*Gayet et al.*, 2006], using the following relationship:

$$D_{\text{eff}} = A \times \text{IWC}/\text{Ext} \quad (6)$$

with D_{eff} expressed in μm, IWC in g m^{-3}, *Ext* in km^{-1}, and $A = 3000$ mm^3 g^{-1}.

[24] The accuracy of the derived microphysical parameters is considerably affected by inherent shortcomings in the probes and data processing. Considering the sampling time of 5 s, the total random uncertainties were estimated as ranging from 75% to 100% for the PMS probe data (see details given by *Gayet et al.* [2002b]). These errors can be drastically reduced by averaging over longer periods.

[25] The accuracies of the in situ measurements reported above could be seriously reduced by the shattering of large ice crystals on probes with shrouded inlets (Polar Nephelometer, CPI and PMS FSSP and 2D-C for instance) [*Korolev and Isaac*, 2005]. *Heymsfield* [2007] modeled the probe responses to different combinations of IWC and large particle concentration. In relatively extreme situations, the results show that the shattering effects could add about 15% to the IWC from the FSSP, while the problem is even greater for extinction and number concentration. *McFarquhar et al.* [2007] experimentally confirm that shrouded inlets may cause particle shattering with a subsequent enhancement of the total concentration of ice crystals, especially at $D < 50$ μm. For particle diameters larger than about 100 μm, the number of shattered particles increases with the concentration of large particles. Techniques have been proposed by *Field et al.* [2003, 2006] to separate genuine small particles from shattering artifacts using ice particle interarrival times (from either Fast-FSSP or 2D-C probes), thus making objective corrections possible. New particle image probes with high pixel resolution may also be used to quantify the contribution of shattering to the particle size distributions and optical properties measured by probes with shrouded inlets (FSSP and Polar Nephelometer for instance). However, these instruments were not available for the present study. The possible effects of ice crystal shattering on the present study will be discussed together with the results below.

4. Comparison of CALIOP Products With Airborne Lidar Profiles and in Situ Observations

[26] In this section, we will first compare CALIOP observations with LNG lidar vertical profiles in terms of (1) attenuated backscatter coefficient and (2) extinction coefficient. Then we will show with details quantitative comparisons of CALIOP retrieved extinction with in situ observations.

4.1. Comparison of CALIOP and LNG Profiles of Attenuated Backscatter Coefficient

[27] Figure 2 displays the vertical profiles of the attenuated backscatter coefficient (ABC) at 1064 nm from CALIOP observations on 16 May (between 47°N and 49.3°N) and on 25 May (between 45.7°N and 48°N). The corresponding LNG observations of the attenuated backscatter coefficient at 1064 nm are plotted above the CALIOP profiles. The horizontal and vertical resolutions are 5 km and 60 m, respectively, for CALIOP data in the troposphere and 1 km and 6 m for LNG. The coincidences between space and airborne observations occurred at 48°N (1333 UT) on 16 May and at 46.5°N (1326 UT) on 25 May.

[28] The results in Figure 2 highlight a close correspondence between the CALIOP and LNG measurements in both cases. However, a few differences are also evident. On 16 May the attenuated backscatter coefficient appears stronger at the cloud top altitude than at the bottom in the airborne observations, whereas the opposite effect is observed in the spaceborne profiles. Such differences are less marked for the 25 May data. In order to quantify these differences, several regions have been identified in both scenes. They are labeled and delimited by rectangles in Figure 2. The CALIOP and LNG ABC profiles (at 532 nm) were averaged over each defined region and with the same vertical resolution (60 m). The results are reported in Figure 3, with dashed lines which represent the model atmospheric density profile. The gray areas correspond to the cirrus layer sampled with the DLR F20. Daytime calibration accuracy is about 10% for CALIOP [*Powell et al.*, 2008] and about 20% for the LNG lidar data. Despite noisy daytime CALIOP profiles, the comparisons of attenuated backscatter profiles in Figure 3 reveal interesting features on geometrical and backscattering cirrus properties which are now discussed:

[29] 1. The cirrus cloud top and base altitudes are determined with a very close agreement. This confirms the accuracies of airborne altitude measurements and of retrieved information from both remote techniques. The technique used by CALIOP algorithms have already been thoroughly described by *Vaughan et al.* [2009]. The boundary detection scheme detects atmospheric features (clouds, aerosols…) considering an extended and contiguous region of enhanced backscatter signal that exceeds significantly an expected molecular value. CALIOP altitudes presented here come from level 2 data products and are determined by this technique. Concerning LNG, two detection boundary schemes were considered, one using a threshold on scattering ratio and a second one which considers a threshold on the signal-to-noise ratio *Chazette et al.* [2001]. As the case we are dealing with consists of cirrus clouds with high scattering ratio, the simple threshold on scattering ratio is used for this study. The exact agreement between CALIPSO and LNG altitudes depend of the threshold value. A scattering ratio of 1 increases the sensitivity but keeps a high level of noise whereas a value of 6 allows us to totally filter out the noise. For this comparison, we chose to lower the level of noise, as we are interested by the general cloud structures as seen in Figures 2 and 3.

[30] 2. Within the cirrus cloud layers, significant differences are found between CALIOP and LNG attenuated backscattering profiles. For 16 May, the region 1 profiles show much larger CALIOP values than LNG (up to 10 times larger). In region 2 the differences are smaller (within 30%), whereas region 3 exhibits systematically larger CALIOP values throughout the entire cloud depth, with a CALIOP/LNG ratio of ~2 in the lower half of the cloud depth. For the 25 May situation in region 2, the two profiles are remarkably well correlated in the upper cirrus layer (between 9.3 and 11.5 km), whereas in the lower cloud layer near 6 km, CALIOP is much larger than LNG (ratio of ~5). Some differences (within 30%) are also observed in region 1.

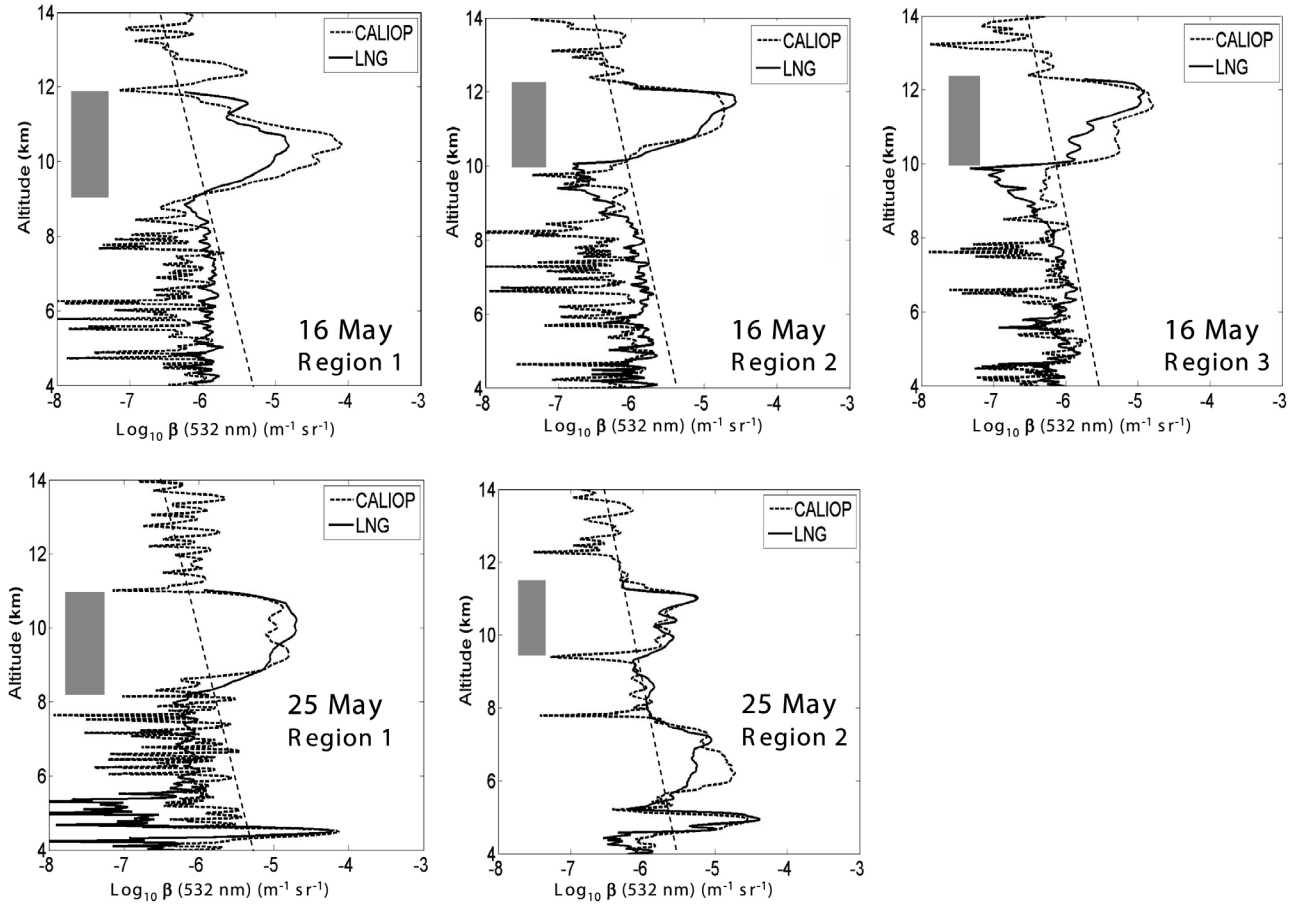

Figure 3. CALIOP and LNG 1064 nm attenuated backscatter profiles averaged over the region of interest identified in Figure 2 for the 16 and 25 May situations. Molecular backscattering is given as dashed lines, normalized above and below the cloud. The gray areas correspond to the cirrus layers sampled by the Deutsches Zentrum für Luft- und Raumfahrt (DLR) F20. For 16 May, the overpass time is 1333 UT, and LNG sampling time periods for regions 1, 2, and 3 are 1321–1325, 1335–1338, and 1339–1343 UT, respectively. For 25 May, the overpass time is 1326 UT, and the LNG sampling time periods are 1328–1331 and 1337–1339 UT for regions 1 and 2, respectively.

[31] These differences may be attributed to changes in cloud properties with time as airborne and spaceborne observations are not exactly coincident. Nevertheless, the small time differences considered (less than 10 min) may mitigate the subsequent uncertainties in the data analysis. During the CIRCLE-2 campaign, the CALIOP lidar was quasi-nadir oriented (0.3° ahead of the nadir direction) whereas the LNG airborne lidar was oriented 3° ahead of nadir pointing. Therefore, the combination of these two remote techniques may give determinant information on the presence of oriented ice crystals, which can induce specular scattering effects according to the angle of observation due to specific ice crystal structures [*Bréon and Dubrulle*, 2004; *Noel and Sassen*, 2005; *Shcherbakov et al.*, 2006]. As a matter of fact, while CALIOP data can be sensitive to specular effects due to pristine ice crystals, LNG are not, because of the tilted beam, and this can explain the larger CALIOP backscattering values. We will compare in the next section the retrieved extinctions that result from the inversion of CALIOP and LNG data in order to introduce the discussion on the assessment of the critical parameters (lidar ratio and multiple-scattering coefficients).

4.2. Comparison of CALIOP and LNG Retrieved Extinctions

[32] The method to retrieve the extinction from LNG data is detailed in Appendix A. To help understand main differences, the results presented in this section show comparisons between CALIOP and LNG extinction retrievals. A more detailed analysis on the underlying assumptions and a step by step comparison of the inversion process applied to airborne and spaceborne data is beyond the scope of this paper and could be the object of a forthcoming issue. We will here limit the comparison to a focused approach.

[33] Figures 4a and 4b show the comparisons between CALIOP and LNG effective extinction determined for 16 May (see region 2 in Figure 3) and 25 May (see region 2 in Figure 3), respectively. We note that fewer data points are available for 25 May because of a shorter in-cloud sequence related to region 2 (see Figure 2). As expected from ABC profiles in Figure 3, a relatively good agreement between CALIOP and LNG is observed on 25 May (slope parameter and correlation coefficient of 1.09 and 0.87, respectively). Because of different fields of view for CALIOP and LNG

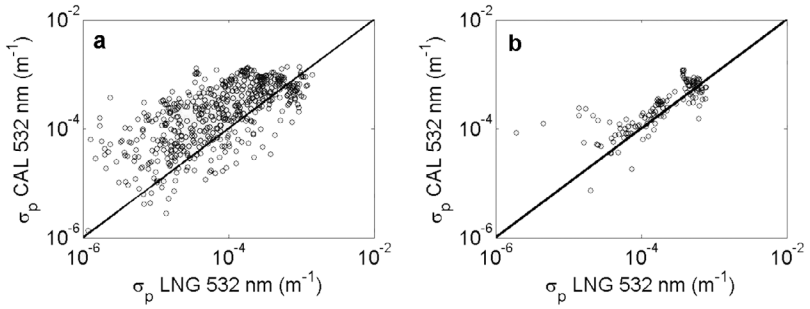

Figure 4. Comparison between CALIOP and LNG retrieved extinctions. For LNG, S_P = 20 sr, η = 0.9, and operational values (level 2) are used for CALIOP. The (a) 16 May (5 min before and after overpass time) and (b) 25 May (3 min after the overpass) cases are shown.

(130 and 5 mrad at 532 nm, respectively) and the observation distance (790 versus 2 to 5 km), the multiple-scattering coefficient should be different for a same target. Nevertheless, the LNG results are obtained with lidar ratio and multiple-scattering factor values close from those of CALIOP operational retrievals in terms of effective lidar ratio ηS (S = 20 sr against 25 sr and η = 0.8 versus 0.6, respectively). Differences may be explained by the fact that both retrievals use statistical and constant values whereas these parameters may significantly change in an unknown way according to horizontal and vertical heterogeneity scales of the cirrus layer. However, all these effects together should not impact the average value and appear to give a better general agreement on 25 May, although for a smaller number of points.

[34] Concerning the 16 May case (see Figure 4a), the data are very dispersed (correlation coefficient of only 0.12) with on the average larger CALIOP extinctions which prevent any quantitative comparison. As previously discussed in section 4.1, the differences observed could be explained by the occurrence of horizontally oriented plates. In the next section, in situ observations will contribute to an exhaustive interpretation of the above remote sensing observations.

4.3. Comparison of CALIOP Extinction Coefficient With in Situ Measurements

[35] Figure 5 displays the vertical profiles of the retrieved extinction coefficient from CALIOP level 2.01 operational cloud profile product for the measurements acquired on (Figure 5a) 16, (Figure 5b) 23, (Figure 5c) 25, and (Figure 5d) 26 May. The CALIOP extinction coefficient is obtained with 5 km and 60 m horizontal and vertical resolutions, respectively. The superimposed red lines are the Falcon flight altitudes of the cloud sequences reported in Table 1.

[36] We recall that the in situ extinction coefficient can be derived from both the Polar Nephelometer and the combined FSSP-300 and CPI measurements. As we will discuss below, cross-correlations performed between extinction measurements obtained from these two different techniques highlight very good results which validate the probe calibrations and the methods of data processing. Indeed, the Polar Nephelometer (PN) extinction will be used in the

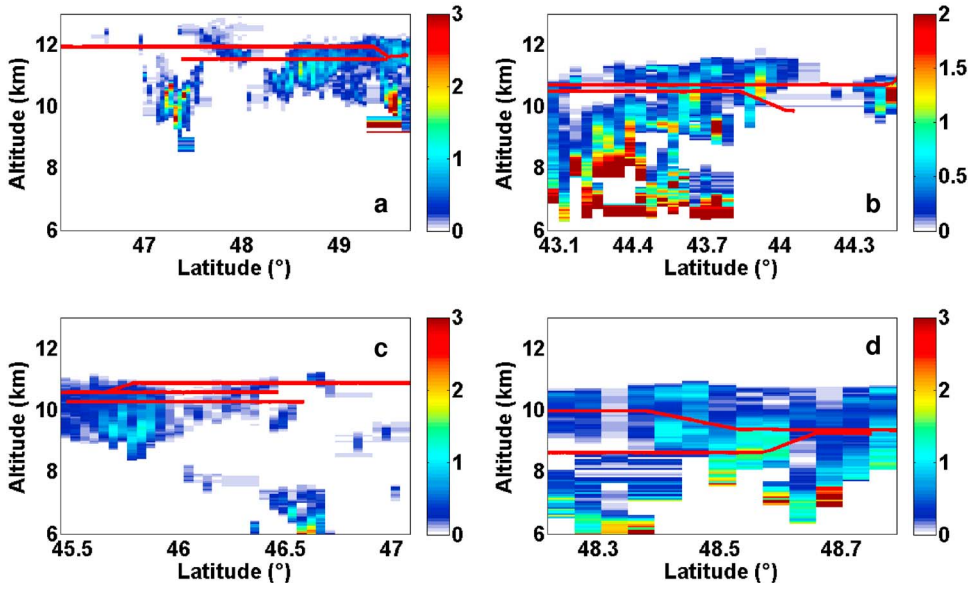

Figure 5. Vertical profiles of the Extinction coefficient from CALIPSO level 2 cloud products (color scale in km^{-1}), for the (a) 16, (b) 23, (c) 25, and (d) 26 May cirrus cases. The synchronized Falcon flight tracks are superimposed with red lines.

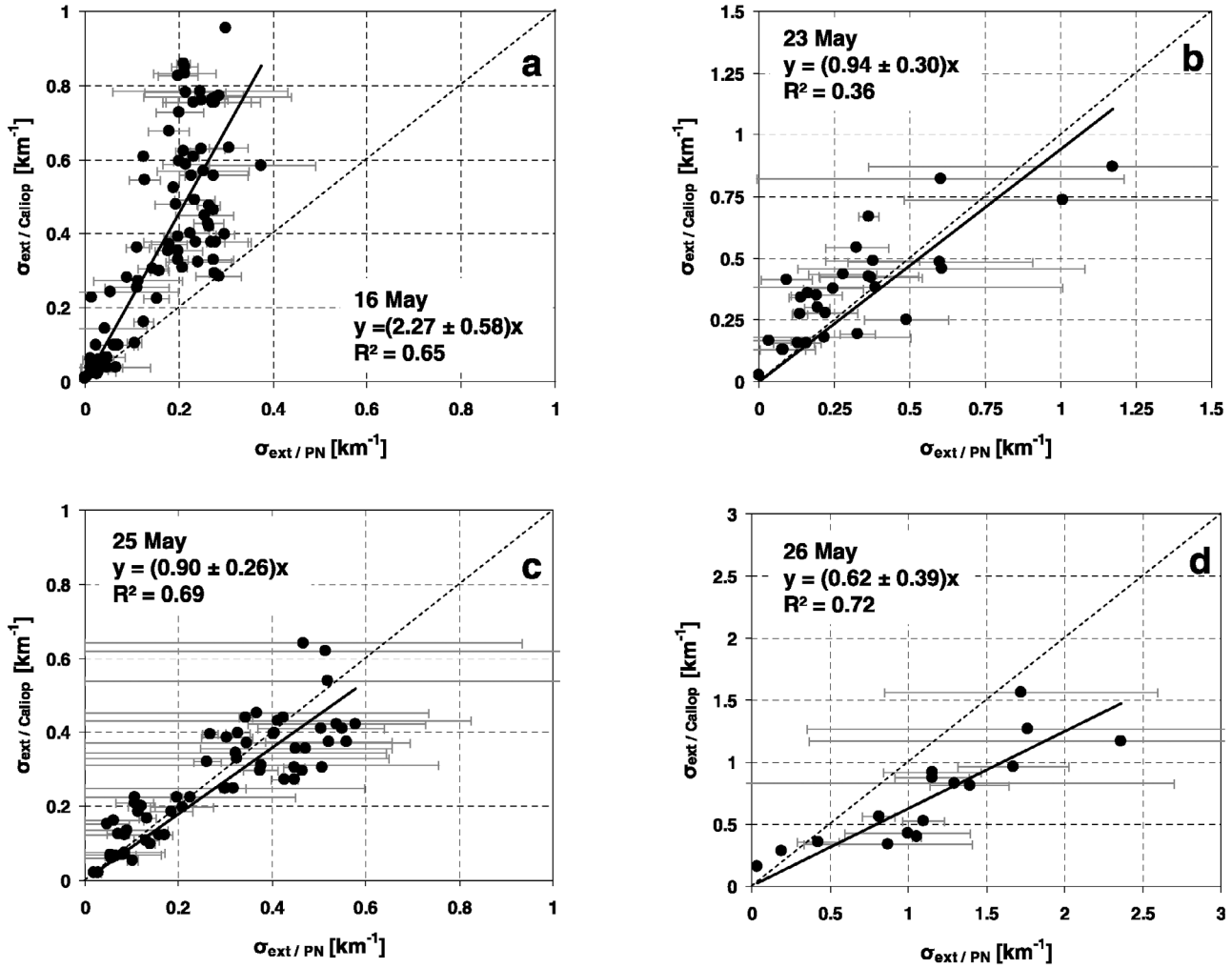

Figure 6. Comparison between extinction coefficients from CALIOP lidar retrievals and from in situ measurements by the Polar Nephelometer for the (a) 16, (b) 23, (c) 25, and (d) 26 May situations. The slope parameters of linear fittings with their uncertainties and correlation coefficients are also indicated.

following. It should be noticed that the in situ observations have been averaged over the horizontal CALIOP pixel resolution (i.e., 5 km (see Figure 5) or about 25 s according to the mean Falcon airspeed). The flight trajectory was first projected onto the CALIOP vertical plane by considering the mean wind advection at the corresponding levels and the time difference between satellite and in situ measurements. This was done to reduce inherent errors in comparing quasi-instantaneous spaceborne observations and aircraft measurements carried out during a much longer duration. Then for each satellite pixel the spatial collocation was realized according to combined corrected latitude-longitude coordinates of the satellite track and the DLR F20 aircraft.

[37] The results of the CALIOP validation are displayed in Figure 6. Figure 6 displays the CALIOP extinction versus the PN extinction for the (Figure 6a) 16, (Figure 6b) 23, (Figure 6c) 25, and (Figure 6d) 26 May cirrus cases. The horizontal bars represent the standard deviation of the in situ extinction, which results from the horizontal cloud variability over 25 s. The examination of the results shows a very good correspondence between the two measurements for the 23 and 25 May situations despite very different situations: outflow cirrus and thin frontal cirrus, respectively. The slope parameters of the linear fits are 0.94 and 0.90, with maximum extinction values of about 1.2 and 0.6 km^{-1}, respectively. The correlation coefficient is much better for 25 May (0.69) than for 23 May (0.36) because of a smaller number of measurements with a larger dispersion.

[38] As for the 16 and 26 May situations, significant differences are evidenced between the two measurements. For the 16 May comparison, systematically larger CALIOP extinctions than PN observations are evidenced (slope parameter of 2.27). Indeed, for CALIOP values in the range from 0.4 km^{-1} to 0.9 km^{-1}, no agreement can be found, since the PN extinctions remain no larger than about 0.25 km^{-1}. In contrast, the 26 May CALIOP values are systematically lower than the in situ observations with a slope parameter of 0.62 and a correlation coefficient of 0.72, and without apparent saturation on either of the signals. We now discuss the interpretation of the measurements in order to explain the differences evidenced on the 16 and 26 May cirrus cases.

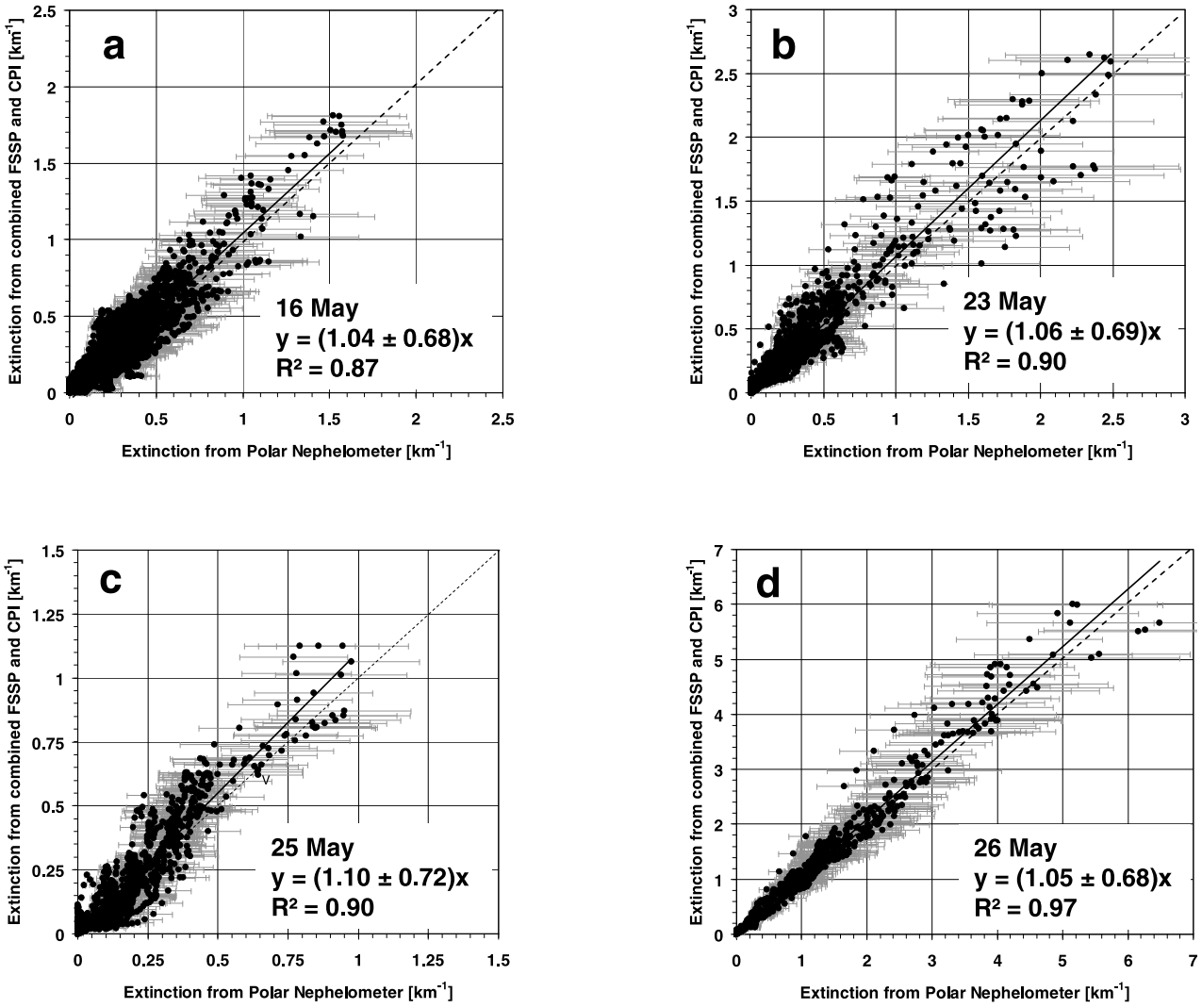

Figure 7. Comparison between extinction coefficients from combined FSSP-300 and CPI instruments and Polar Nephelometer probe for the (a) 16, (b) 23, (c) 25, and (d) 26 May situations. The slope parameters with their uncertainties and correlation coefficients are reported. Horizontal gray bars represent the 25% uncertainties on Polar Nephelometer measurements.

4.3.1. The 16 May Cirrus Case

[39] We recall this situation concerns a frontal thin cirrus over ocean like the 25 May cirrus case with quite similar geometrical properties (see Figures 5a and 5c) but with lower temperatures (−56°C to −59°C against −50°C to −54° C; see Table 1). The very coherent nature of the in situ observations argues strongly against any systematic errors in the in situ measurements when comparing the extinction relationships in Figure 6. As a matter of fact, Figure 7 reports comparisons between the extinction coefficients from the combined FSSP-300 and CPI instruments and the Polar Nephelometer probe for the (Figure 7a) 16, (Figure 7b) 23, (Figure 7c) 25, and (Figure 7d) 26 May situations. Cloud data at 1 Hz frequency are shown in Figure 7. The results emphasize that the two measurements fit very well for the four cirrus cases, with quasi-identical slope parameters of the linear fits (1.06 ± 0.03) and correlation coefficients close to 0.9. Likewise, very similar particle size distributions and extinction distributions are observed for the 16 and 25 May situations, as reported in Figures 8a and 8b, respectively. Figures 8a and 8b represent the particle size and extinction distributions measured by the FSSP-300 and CPI probes and are averaged over the cloud sequences for each of the four cirrus cases. Table 2 reports the mean values of the microphysical parameters. Considering the 16 and 25 May observations, because only few ice particles larger than 100 μm in diameter were observed (0.5 and 1.5 L^{-1}, respectively; see Table 2), with no ice crystals larger than about 350 μm, we may expect that the shattering effects are probably not very important and are not greater than the usual random uncertainties (i.e., 25% for the PN extinction [see *Gayet et al.*, 2002b, Table 1]. However, hypothesizing shattering occurrence, the effects on measurements (on both FSSP-300+CPI and Polar Nephelometer) should be of the same order for the 16 and 25 May situations because of the similarities of the size distributions.

[40] In conclusion, the close agreement between the in situ measurements from 16 and 25 May strongly suggests that

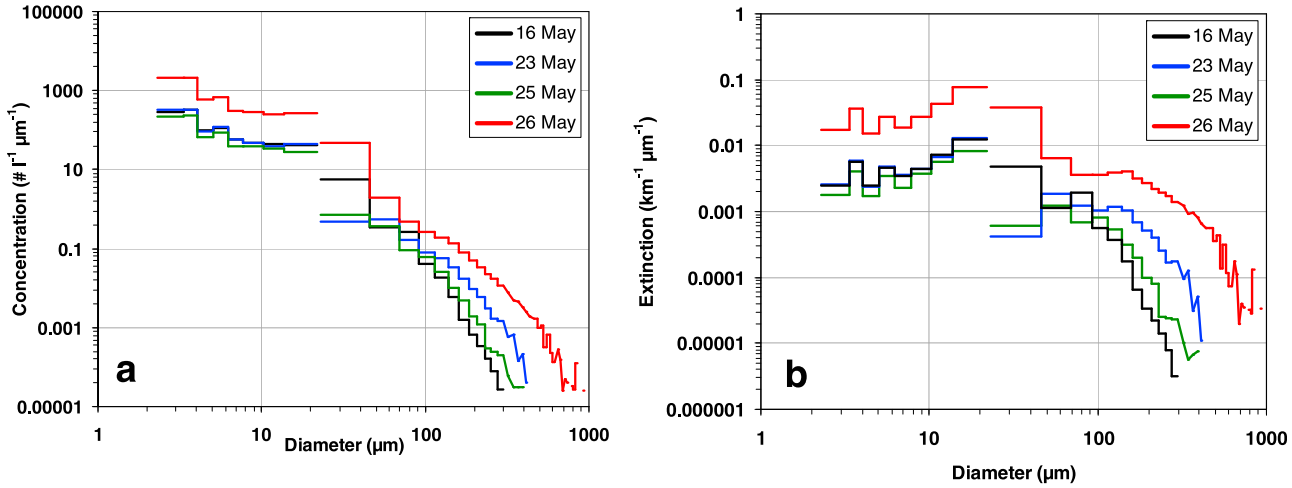

Figure 8. (a) Particle size distributions and (b) particle extinction coefficient distributions determined by the FSSP-100 and CPI probes as a function of diameter and averaged over the cloud sequences related to the 16, 23, 25, and 26 May cirrus cases.

the disparities seen in Figure 6a are not due to errors in the Polar Nephelometer data, but should instead be attributed to overestimates generated by the CALIOP retrieval. Therefore, one possible explanation may be the preferential orientation of the planar-shaped ice crystals, which can provoke a dramatically stronger lidar backscatter than would be expected for randomly oriented ice particles [*Sassen*, 1980; *Hu et al.*, 2007]. A stronger extinction value will be retrieved in that case. In order to give arguments to support this hypothesis, the CPI ice particle shape classifications (represented for number, surface, and mass percentages) are displayed in Figure 9. The comparison of the results shown in Figures 9a (16 May) and 9c (25 May) clearly highlights significant differences in dominant crystal shape within the temperature (or altitude) domains in which the CALIOP comparisons have been made. Pristine-plate ice crystals dominate the ice crystal shape during the 16 May cirrus case, as clearly evidenced by CPI examples of ice crystal images in Figure 9a, whereas for the 25 May situation (Figure 9c) the main shape of the particles is irregular with some bullets and plates (see examples of ice crystals on Figure 9c). Pristine-plate ice crystals with sizes up to 300 μm could be horizontally oriented [*Bréon and Dubrulle*, 2004] and may therefore explain the poor extinction comparison for the 16 May data.

[41] These findings nicely confirm the interpretation of the comparison results between CALIOP and LNG measurements discussed in section 4.1. A signature of oriented ice crystals is evidenced in region 2 (16 May situation; see Figure 3), particularly in the half lower part of the cirrus layer, which was sampled by the DLR F20 aircraft during the second cloud sequence (see Table 1). On the contrary, no signatures of oriented particles are found in the cirrus layer sampled by the DLR F20 during the 25 May situation, as evidenced from LNG observations.

[42] The preferential orientation signature could also be verified from the diagram of the CALIOP layer-integrated attenuated backscatter (γ') versus the layer-integrated depolarization ratio (δ) as proposed by *Hu et al.* [2007] and *Cho et al.* [2008]. These diagrams are reported in Figure 10. The results in Figures 10a (16 May) and 10c (25 May) clearly show the signatures of both the low-level water clouds and the randomly oriented ice crystals in cirrus clouds [see *Hu et al.*, 2007]. The observation of pristine-plate ice crystals at the CALIOP validation levels during the 16 May cirrus case are consistent with the location of the data points in Figure 10a at the upper left portion of the scatterplot, which corresponds to horizontally oriented ice crystals as hypothesized by *Hu et al.* [2007]. The number of pixels is poor due to the small CALIPSO data set available during these limited cloud sequences. Nevertheless, this feature is not observed for 25 May, and this would confirm our findings about the orientation effect of particles. The boundary stratiform clouds over the sea on the 16 and 25 May situations were detected by CALIOP because of the relatively low cirrus optical depth (~0.5) and fractional

Table 2. Mean Values of Microphysical Parameters Obtained During Cirrus Cloud Sequences[a]

Day (in 2007)	Particle Conc. (cm^{-3})	Particle Conc. ($D > 25$ μm) (L^{-1})	Particle Conc. ($D > 100$ μm) (L^{-1})	IWC (mg m^{-3})	IWC ($D > 25$ μm) (mg m^{-3})	Extinction (km^{-1})	Extinction ($D > 25$ μm) (km^{-1})	D_{eff} (μm)	D_{eff} ($D > 25$ μm) (μm)
16 May	1.0	3.7	1.9	1.7	1.1	0.20	0.013	17.6	27.
23 May	1.0	53.7	7.6	7.0	4.9	0.33	0.18	40.9	70.
25 May	0.9	26.1	3.3	2.8	2.3	0.22	0.08	20.8	43.
26 May	3.9	109.0	37.8	36.9	21.7	1.18	0.58	79.5	115.

[a]Reported are the total ice particle concentration, ice water content (IWC), extinction coefficient, and effective diameter. The parameters labeled with $D > 25$ μm and $D > 100$ μm are calculated for particle diameter larger than the indicated values.

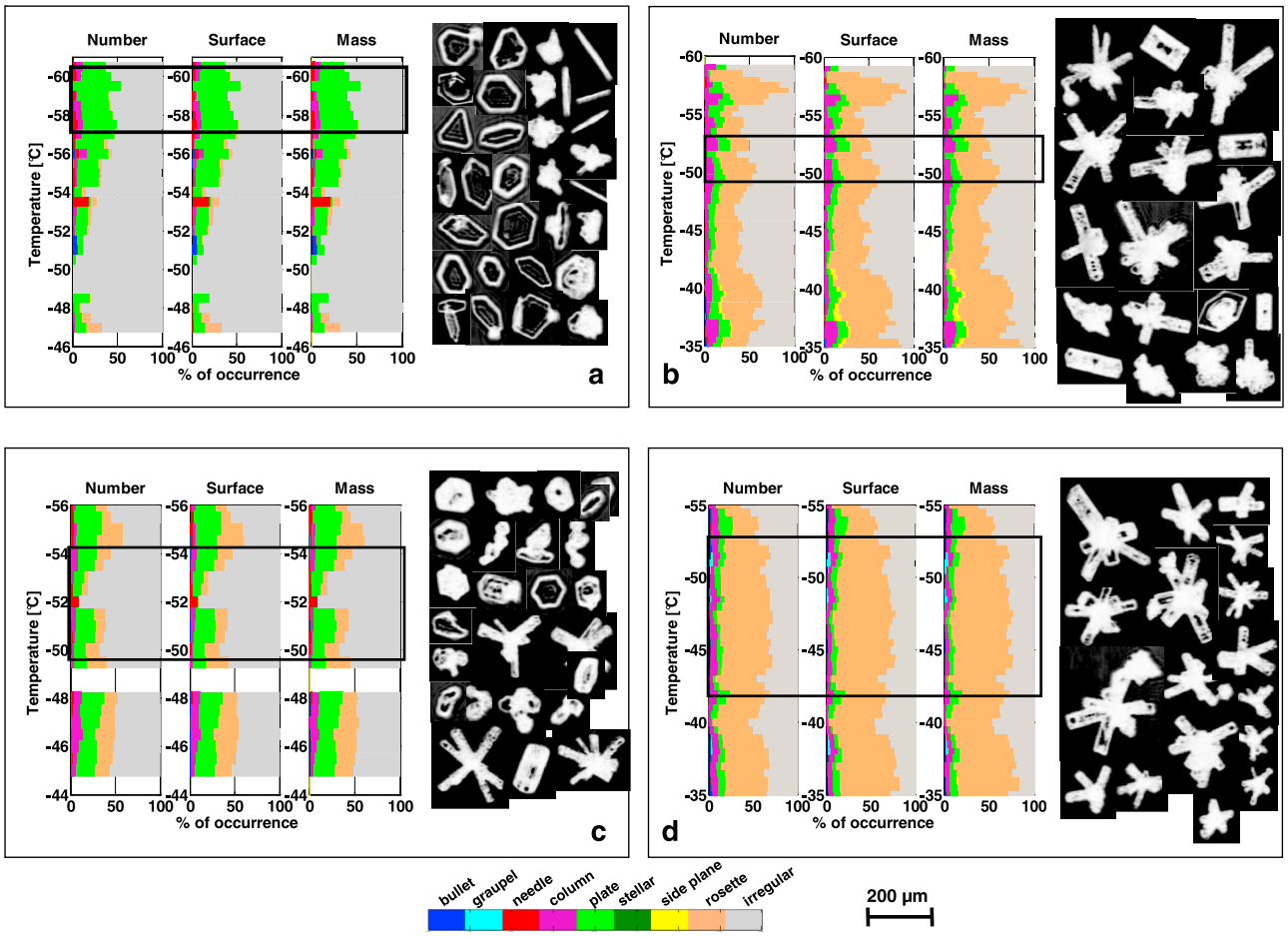

Figure 9. CPI classification of the ice particle shape in number, surface, and mass percentages for the (a) 16, (b) 23, (c) 25, and (d) 26 May situations. The rectangles represent the temperature domains in which the CALIOP and in situ comparisons have been made.

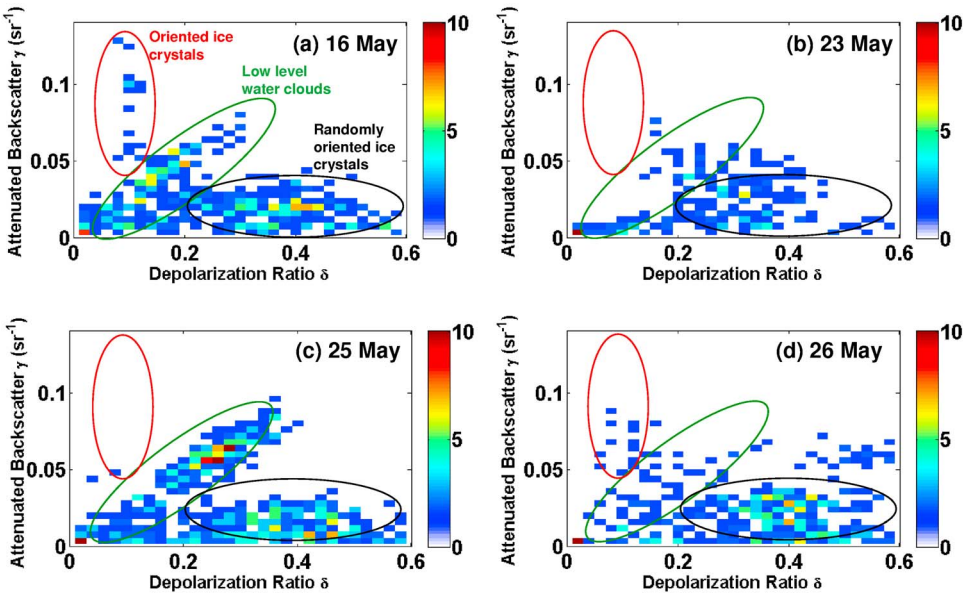

Figure 10. Diagram of $\gamma' - \delta$ from CALIOP data for the (a) 16, (b) 23, (c) 25, and (d) 26 May situations. Color scale represents the frequency of occurrence, and the resolutions of each pixel are $\Delta\gamma' = 0.004$ sr^{-1} and $\Delta\delta = 0.02$.

structure of the cirrus layers during the considered flight sequences. This feature is not observed during the outflow cirrus cases shown in Figures 10b and 10c. We note in passing that no more clouds were observed between the cirrus and the stratiform cloud layers for these two case studies.

[43] The presence of horizontally oriented plates in cirrus clouds is attested to by numerous previous studies from spaceborne reflectance observations [*Chepfer et al.*, 1999; *Bréon and Dubrulle*, 2004; *Noel and Chepfer*, 2004]. On a global scale, this feature is apparent for roughly half of the cirrus clouds observed by Polarization and Directionality of the Earth Reflectances (POLDER) [*Bréon and Dubrulle*, 2004], and more frequently at high latitude. As a result, larger extinction values and subsequently larger cirrus optical depths should be retrieved from CALIOP observations. In order to avoid such biases in the CALIPSO retrievals, since November 2007, the CALIOP laser beam is tilted of 3° ahead of the nadir pointing direction. On the other hand, the climatology of the oriented plate ice crystals is of great interest regarding the optical and radiative properties of cirrus clouds. Direct retrieval of optical depths using backscatter from water clouds or surface echoes [*Hu et al.*, 2007; *Josset et al.*, 2008] is expected to provide new insights for the analysis of these properties.

4.3.2. The 26 May Cirrus Case

[44] We recall that the 26 May case addresses outflow cirrus like the 23 May situation, but with a larger optical depth, since the PN extinction reaches 2.5 km^{-1} against 1.2 km^{-1} (see Figures 6d and 6b, respectively). As in the previous discussion, the coherence of the in situ observations eliminates concerns about systematic errors in the in situ measurements when comparing the extinction relationships in Figure 6d. Quasi-identical slope parameters (1.06 and 1.05) are found for the two considered situations (see Figures 7b and 7d). Likewise, quite similar ice crystal shape distributions are observed for the both outflow cirrus cases within the temperature (or altitude) domains in which the CALIOP comparisons have been made. The dominant shape (bullet-rosette) is observed about 30% and 50% of the time (in number, surface, and mass distributions) for 23 and 26 May, respectively, as exemplified by the CPI images shown in Figures 9b and 9d.

[45] The extinction results retrieved from the CALIOP data are strongly dependent on the lidar ratio and multiple-scattering coefficient, and any cause for possible variability of these parameters must be examined. Because the lidar ratio depends on the shape, size, and orientation of the ice particles [*Chen et al.*, 2002], the observation of rather similarly shaped (nonplanar) ice crystals allows us to assume that any crystal-shape effect could be neglected. However, compared to the 23 May case, significantly larger ice particle sizes and extinction coefficients are evidenced for the 26 May situation (see Figures 8a and 8b and Table 2) with a consequently greater optical depth. If the CALIOP lidar ratio is changed from 25 to 40 sr, the CALIOP extinction coefficient will increase by a factor of 1.6 (40/25), and the linear fit in Figure 6d becomes very close to unity ($0.62 \times 1.6 = 0.992$). Therefore the CALIOP data would be more consistent with the in situ observations. A lidar ratio value of 40 sr is within the upper part of the one sigma variation from the *Sassen and Comstock* [2001] results at the corresponding optical depth. Nevertheless, for clouds with high optical depths the multiple-scattering effect lowers the effective lidar ratios compared with single-scattering condition [*Chen et al.*, 2002]. Because CALIOP and PN extinctions agree well for the 23 May situation, this implies that the lidar ratio and multiple-scattering values of 25 and 0.6 are suitable for this case. Therefore with a similar ice crystal population but with a larger extinction (and subsequent optical depth) the multiple-scattering coefficient and the lidar ratio would have lower values according to the trend from *Sassen and Comstock* [2001], a conclusion which is contradictory with our 26 May observations.

[46] As already indicated, large ice crystals (up to 800 μm) are measured during the 26 May situation (see Figure 8). Therefore, the contamination of the FSSP-300, CPI, and Polar Nephelometer measurements by the shattering of ice crystals could likely be more important than for the other cases, since the concentration of particles with diameter larger 100 μm is significant (10 L^{-1}, see Table 2). It is conceivable that the effects of shattering depend on the design of the probe inlet [*Heymsfield*, 2007]. The extinction coefficients are inferred from the FSSP-300 + CPI and from the Polar Nephelometer probes, which all have very different inlet designs (for instance, inlet diameters of 40, 23, and 10 mm, respectively). The hypothesis that the shattering of large ice crystals affects the FSSP-300+CPI and PN measurements in the same way, or with a same efficiency, appears unlikely. This is supported by the consistency of comparison results between extinctions calculated from two different techniques (FSSP-300 + CPI and PN) and obtained during very different microphysical cloud properties (rather sharp and broad size distributions; see Figure 8a). This would appear unlikely if artifacts dominate the measurements. Otherwise, with regard to the very good agreement between CALIOP and PN observations when small ice crystals are evidenced (23 and 25 May), the subsequent shattering contamination of the FSSP-300 and PN measurements in presence of more numerous and larger ice crystals seems a plausible explanation for the larger PN values (38% larger than CALIOP extinction values) evidenced in Figure 10d. In conclusion, the relative importance of the effects of shattering of ice crystals on the in situ measurements (the extinction coefficient in our case) remains an open question. For example, contradictory conclusions have been drawn about the reliability of the Cloud Integrating Nephelometer (CIN) [*Gerber et al.*, 2000] with regard to the shattering contamination. *Garrett* [2007] suggested an absence of sensitivity to shattering of particles on the CIN aperture. Comparisons of lidar volume extinction from the airborne Cloud Physics Lidar (CPL) and in situ CIN extinction measurements have shown very good agreement [*Noel et al.*, 2007].

[47] Another plausible explanation for the differences observed could be the weak spatial and temporal coincidence with the satellite observations due to (1) the restricted flight area over Germany by the Air Traffic Control Authority, which permitted only rather short flight legs under the satellite trace (see Figure 5d, which shows cloud sequences of 0.6° latitude long against more than 2° for the other cases); (2) the internal structure of the cirrus clouds, which varied very rapidly during the time of observations [*Protat et al.*, 2009]; indeed the outflow cirrus sampled on

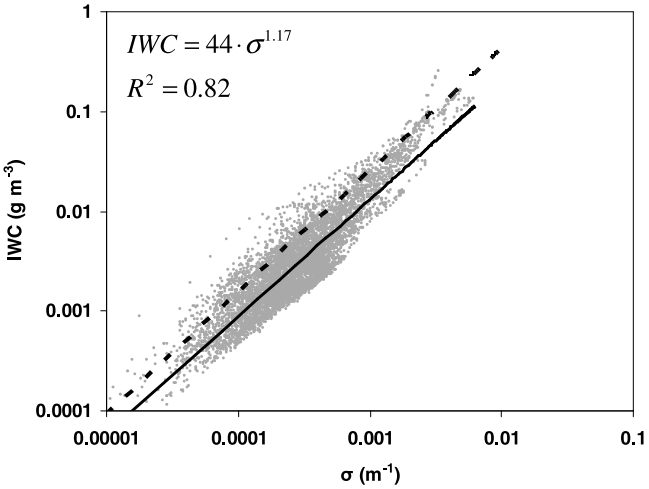

Figure 11. Relationship between ice water content and extinction coefficient derived from in situ data set presented in this study. Individual data points are plotted with the power law curve (full line). The dashed line represents the power law proposed by *Heymsfield et al.* [2005].

26 May topped the main convective system, whereas during the 23 May situation the sampled cirrus resulted from an advected anvil, as seen in Figure 5b; and (3) the horizontal inhomogeneities in the cloud properties: these could be estimated from the standard deviation (or variance) when averaging the 1 Hz (or ~200 m horizontal resolution) Polar Nephelometer extinction over the CALIOP pixel resolution (5 km); the standard deviations (see the error bars in Figure 6) clearly show large values for the 26 May case (Figure 6d), with the one sigma variation overlapping the 1:1 slope.

5. IWC Extinction and Temperature-Effective Diameter Relationships

[48] The in situ measurement data set obtained during the cloud sequences reported above can also be used in order to assess the relationship between the ice water content (IWC) and the extinction coefficient. Such a relationship is a key issue for deriving IWC, and therefore the effective diameter (see equation (1)), for cirrus clouds from retrieved extinction from spaceborne observations. Figure 11 represents the ice water content (IWC) versus the extinction coefficient (σ), both parameters being calculated from the FSSP-300 and CPI instruments. Cloud data at 1 Hz frequency are shown in Figure 11. The results show a linear tendency when plotted in log-log scales, and the power law curve fitted through the data is the following:

$$IWC = 44\sigma^{1.17} \tag{7}$$

with IWC and σ expressed in g m^{-3} and m^{-1}, respectively. The correlation coefficient (0.82) reflects the scatter about the best fit line in Figure 11. The coefficient of variation (i.e., the ratio of the standard deviation about the best fit line to the mean) changes significantly according to the extinction coefficient. It decreases from about 70% to 20% when the extinction ranges from 10^{-3} km^{-1} to 10^{-1} km^{-1}. These values give rough estimates on IWC retrieval uncertainties as a function of the extinction coefficient. *Heymsfield et al.* [2005] found a slightly different relationship (see dashed line in Figure 11), probably due to a more extended domain of observations in terms of temperature (−20°C to −70°C versus −38°C to −60°C in this study) and subsequent larger σ and IWC values. Figure 12 displays the relationship between the effective diameter (D_{eff}) and the temperature. We recall the effective diameter is estimated from IWC and σ in situ measurements by using equation (6). Mean values and standard deviations were calculated over 2°C intervals. The full line represents the exponential law curve which fit the data with the following relationship:

$$D_{\text{eff}} = 18.2 + 185 \cdot e^{\left(\frac{-23.07}{T+61.7}\right)} \tag{8}$$

with D_{eff} and T expressed in μm and °C, respectively. The correlation coefficient is 0.98. The exponential law represents the nonlinear D_{eff}-T relationship with the asymptotical value for D_{eff} (18 μm) at lower temperatures.

6. Conclusions

[49] This paper presents a comparison of quasi-collocated CALIPSO observations and airborne lidar (LNG) and in situ cirrus cloud measurements carried out during the CIRCLE-2 experiment in May 2007. The objective of this comparison is to assess the reliability of the algorithms that derive secondary products from CALIOP and to identify potential problems inherent to these retrieval techniques.

[50] Comparisons between CALIOP attenuated backscatter coefficient and airborne LNG lidar observations reveal either a close agreement or significant differences according to the cirrus situations. Specular effects due to oriented pristine ice crystals are hypothesized to explain large CALIOP backscattering values compared to LNG observations. The CALIOP level 2 extinction products were com-

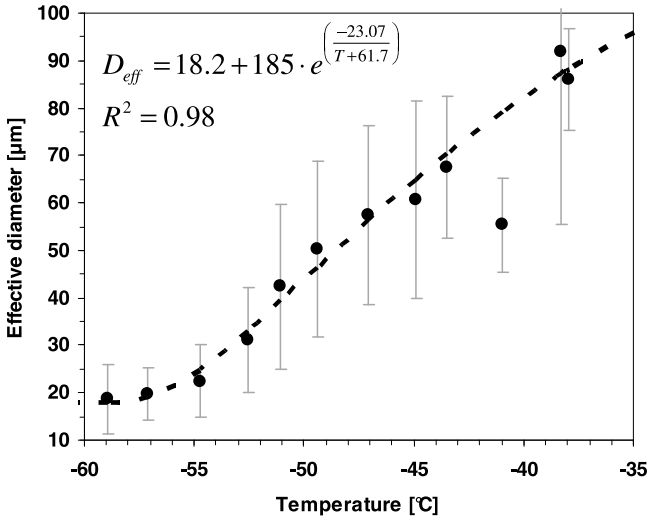

Figure 12. Relationship between the effective diameter and the temperature. Mean values and standard deviations were calculated over 2°C intervals. The full line represents the exponential law curve which fits the data.

pared to the in situ extinction coefficients derived from the Polar Nephelometer during four cirrus cloud situations that included thin cirrus layers and outflow cirrus. In total, nine cloud sequences have been selected for comparison purposes, representing about 130 min of quasi-collocated observations. Despite very different conditions, the results show very good agreement between the extinction observations for two situations: thin frontal cirrus and outflow cirrus. The slope parameters of the linear fits are 0.90 and 0.94 and confirm the validation of the CALIOP level 2 extinction retrieval product in cirrus clouds with extinction coefficients no larger than about 1 km^{-1} and with irregular-shaped ice crystals. The values of the correlation coefficients (0.69 and only 0.36) are explained by inherent and rather large random uncertainties due to the validation procedure from in situ measurements, i.e., (1) the very large differences in lidar beam volume and the sampling volume of in situ cloud measurement instruments (ratio of $\sim 10^8$), (2) comparisons made between quasi-instantaneous spaceborne observations and aircraft measurements that are carried out during a much longer duration during which the cloud properties may change significantly, and (3) the assumption that the natural time variability of the cirrus cloud properties is of the same order of the measured horizontal variability.

[51] In thin frontal cirrus with temperatures ranging from −56°C to −59°C, systematically larger CALIOP extinctions were evidenced with regard to the in situ observations. Pristine-plate ice crystals with sizes up to 300 μm that could be horizontally oriented are evidenced from the images of the CPI instrument and may therefore explain this particular feature. These findings account for the larger CALIOP attenuated backscatter coefficients (when compared to the LNG measurements) that are evident in well-identified parts of the cirrus layers that were sampled by the DLR F20. The preferential crystal orientation signature appears to be further verified from the CALIOP diagram of the layer attenuated backscatter (γ') versus the layer depolarization ratio (δ). In order to avoid subsequent biases in CALIPSO retrieval products as reported in this study, the CALIOP laser beam has been tilted 3° ahead of the nadir direction since November 2007. On the other hand, an extended climatology of the oriented plate ice crystals would have been of great interest regarding the microphysical and radiative properties of cirrus clouds.

[52] In rather dense outflow cirrus, the CALIOP extinctions are systematically lower than the in situ observations; (PN extinction values are larger on the average by 38%). The consistency of comparison results between extinctions calculated from two different techniques (FSSP-300 + CPI and PN) and obtained during very different microphysical cloud properties (rather sharp and broad size distributions) would appear to minimize or even eliminate the effects of contamination of the in situ measurements by the shattering of large ice crystals on probe tips. Otherwise, with regard to the very good agreement between CALIOP and PN observations, when small ice crystals are present (see the previous cirrus cases), the subsequent shattering contamination of both the in situ measurement techniques in presence of more numerous and larger ice crystals seems a plausible explanation for the PN large extinction values. In conclusion, the relative importance of the effects of shattering of ice crystals on in situ measurements (the extinction coefficient in our case) remains an open question. Another plausible explanation for the differences observed could be the weak spatial and temporal coincidence with the satellite observations due to rather rapid variations of the cirrus properties associated to restricted flight legs under the satellite track. Finally, the data set of in situ measurements obtained during the cloud sequences reported in this study are used in order to assess the relationships between the ice water content (IWC), the extinction coefficient, and effective diameter in the observed range of experienced temperature from −38°C to −60°C.

[53] This paper focused on a few case studies of collocated observations from CALIPSO and airborne instruments in thin frontal and in upper parts of outflow cirrus clouds with rather small extinction values (<2 km^{-1}). Inherent to this airborne strategy, the results are affected by two significant limitations: (1) the low statistical representation of the results due to the difficulties in collocating different measurements separated in time and space and (2) the in situ measurement shortcomings due to unknown ice shattering effects when large ice crystals are present.

[54] In conclusion, and because our results address a very limited range of cirrus conditions (thin clouds with irregular particles), the assessment of the algorithms that derive secondary products from CALIOP is restricted to these conditions. In order to identify potential problems in retrieved satellite data, additional observations should be obtained with new in situ instruments designed to reduce the contamination of the measurements by shattering effects. These observations should include cirrus with dense optical depths (<3) at different temperatures and different dominant particle shapes.

Appendix A: LNG Extinction Retrieval Method

[55] Lidar inversion allows us to retrieve extinction from backscatter using a nonlinear process. The error propagation coming from a small difference of calibration may strongly weaken the meaning of the airborne and space lidar comparison. Therefore, as we are concerned with CALIPSO validation and as the operational product is based on the operational calibration, we first need to match LNG calibration with CALIOP calibration prior to the comparisons (this operation is performed only for the inversion process). LNG attenuated backscatter coefficient and CALIOP level 1 have been interpolated on the grid of the level 2 profile of the CALIPSO product. The vertical resolution is 60 m, and the horizontal resolution is 5 km. The difference between the two data sets for noncloudy air is expected to be small, as the different off nadir angle and different multiple scattering should not lead to different backscatter values in this case. This is no longer true for clouds, in which difference in backscattering has been already evidenced: larger backscattering coefficient for space observations at nadir in the presence of ice crystal plates and due to larger multiple scattering.

[56] Considering the sensitivity of inversion, it is important to apply the same algorithm to the airborne and spaceborne data set. A simple approach is used to inverse both airborne and spaceborne lidar data. The agreement of our inversion procedure with the operational retrievals has been checked. The particulate effective extinction ($\eta\sigma_p$) can

be expressed as a function of particulate attenuated backscatter coefficient β_p:

$$\eta\sigma_p = \frac{\eta S_p \beta_p T_p^2}{1 - \eta S_p \int \beta_p T_p^2 dr} \quad \text{(A1)}$$

with T_p^2 the particulate two-way transmittance.

[57] The word "effective" refers to the same quantities weighted by the multiple-scattering coefficient (η). The inversion procedure is a simple iterative process (20 iterations). As long as the iteration results remain below the instability threshold (i.e., S_p stays low which is the case for CALIPSO operational product), there is convergence, and if n refers to the number of iteration performed, the effective extinction is retrieved according to the following equations:

$$\left[\beta_p T_p^2\right]_n = \mathrm{ABC} \times T_{o_3}^{-2} T_M^{-2} - \left[\beta_M T_p^2\right]_n \leq \beta_p T_p^2 \quad \text{(A2)}$$

$$\left[\eta\sigma_p\right]_n = \frac{\eta S_p \left[\beta_p T_p^2\right]_{n-1}}{1 - \eta S_p \int \left[\beta_p T_p^2\right]_{n-1} dr} \text{ with } \left[\tau_p\right]_0 = 0, \left[T_p^2\right]_0 = 1 \quad \text{(A3)}$$

where ABC is the measured attenuated backscatter coefficient, τ_p is the optical thickness, β_M is the molecular attenuated backscatter, and T_p^2 is the molecular two-way transmittance.

[58] **Acknowledgments.** This work was funded by the Centre National d'Etudes Spatiales (CNES) and by a grant from the CNRS/INSU. The contribution of Deutsches Zentrum für Luft- und Raumfahrt (DLR) as well as a large part of Falcon flight hours was funded in the framework of the DLR PAZI-2 project. We thank the members of DLR and Service des Avions Français Instrumentés pour la Recherche en Environnement (SAFIRE) who organized the experiment management and aircraft operations. We are grateful to A. Dörnbrack (DLR) for providing meteorological analysis from the ECMWF model. We would like to acknowledge NASA Langley Research Center Atmospheric Science Data Center, as well as ICARE Center (http://www.icare.fr) in Lille for the CALIPSO data. We acknowledge C. Gourbeyre and J-F. Fournol (LaMP) and B. Weinzierl and H. Rüba (DLR) for their active participation in the experiment. We would like to acknowledge M. Vaughan for fruitful discussion on CALIPSO inversion algorithm and his helpful comments on the manuscript. Anonymous reviewers made important comments that strengthened the manuscript.

References

Baker, B. A., and R. P. Lawson (2006), Improvement in determination of ice water content from two-dimensional particle imagery. Part I: Image to mass relationships, *J. Appl. Meteorol.*, *45*(9), 1282–1290, doi:10.1175/JAM2398.1.

Barker, H. W., A. V. Korolev, D. R. Hudak, J. W. Strapp, K. B. Strawbridge, and M. Wolde (2008), A comparison between CloudSat and aircraft data for a multilayer, mixed-phase cloud system during the Canadian CloudSat-CALIPSO validation project, *J. Geophys. Res.*, *113*, D00A16, doi:10.1029/2008JD009971.

Baumgardner, D., J. E. Dye, B. W. Gandrup, and R.G. Knollenberg (1992), Interpretation of measurements made by the Forward Scattering Spectrometer Probe (FSSP-300) during the airborne arctic stratosphere expedition, *J. Geophys. Res.*, *97*(D8), 8035–8046.

Bissonnette, L. R. (1996), Multiple-scattering lidar equation, *Appl. Opt.*, *35*, 6449–6465, doi:10.1364/AO.35.006449.

Bourassa, A. E., D. A. Degenstein, R. L. Gattinger, and E. J. Llewellyn (2007), Stratospheric aerosol retrieval with optical spectrograph and infrared imaging system limb scatter measurements, *J. Geophys. Res.*, *112*, D10217, doi:10.1029/2006JD008079.

Bréon, F. M., and B. Dubrulle (2004), Horizontally oriented plates in clouds, *J. Atmos. Sci.*, *61*, 2888–2898, doi:10.1175/JAS-3309.1.

Chazette, P., C. David, J. Lefrere, S. Godin, J. Pelon, and G. Mégie (1995), Comparative lidar study of the optical, geometrical and dynamical properties of the stratospheric post-volcanic aerosols following the eruption of El-Chichon and Mount Pinatubo, *J. Geophys. Res.*, *100*(D11), 23,195–23,207, doi:10.1029/95JD02268.

Chazette, P., J. Pelon, and G. Megie (2001), Determination by spaceborne backscatter lidar of the structural parameters of atmospheric scattering layers, *Appl. Opt.*, *40*(21), 3428–3440, doi:10.1364/AO.40.003428.

Chen, W. N., C. W. Chiang, and J. B. Nee (2002), Lidar ratio and depolarisation ratio for cirrus clouds, *Appl. Opt.*, *41*(30), 6470–6476, doi:10.1364/AO.41.006470.

Chepfer, H., G. Brogniez, P. Goloub, F. M. Bréon, and P. H. Flamant (1999), Observations of horizontally oriented ice crystals in cirrus clouds with POLDER-1/ADEOS-1, *J. Quant. Spectrosc. Radiat. Transf.*, *63*, 521–543, doi:10.1016/S0022-4073(99)00036-9.

Cho, H.-M., P. Yang, G. W. Kattawar, S. L. Nasiri, Y. Hu, P. Minnis, C. Trepte, and D. Winker (2008), Depolarization ratio and attenuated backscatter for nine cloud types: Analyses based on collocated CALIPSO lidar and MODIS measurements, *Opt. Express*, *16*(6), 3931–3948, doi:10.1364/OE.16.003931.

Eichler, H., A. Ehrlich, M. Wendisch, G. Mioche, J.-F. Gayet, M. Wirth, C. Emde, and A. Minikin (2009), Influence of ice crystal shape on retrieval of cirrus optical thickness and effective radius: A case study, *J. Geophys. Res.*, *114*, D19203, doi:10.1029/2009JD012215.

Field, P. R., R. Wood, P. R. A. Brown, P. H. Haye, E. Hirst, R. Greenaway, and J. A. Smith (2003), Ice particle interarrival times measured with a Fast FSSP, *J. Atmos. Ocean. Technol.*, *20*, 249–261.

Field, P. R., A. J. Heymsfield, and A. Bansemer (2006), Shattering and interarrival times measured by optical array probes in ice clouds, *J. Atmos. Oceanic Technol.*, *23*, 1357–1371, doi:10.1175/JTECH1922.1.

Garrett, T. J. (2007), Comments on "Effective radius of ice cloud particle populations derived from aircraft probes," *J. Atmos. Oceanic Technol.*, *24*, 1495–1503, doi:10.1175/JTECH2075.1.

Gayet, J.-F., O. Crépel, J.-F. Fournol, and S. Oshchepkov (1997), A new airborne Polar Nephelometer for the measurements of optical and microphysical cloud properties. Part I: Theoretical design, *Ann. Geophys.*, *15*, 451–459, doi:10.1007/s00585-997-0451-1.

Gayet, J.-F., S. Asano, A. Yamazaki, A. Uchiyama, A. Sinyuk, O. Jourdan, and F. Auriol (2002a), Two case studies of continental-type water and maritime mixed-phased stratocumuli over the sea. Part I: Microphysical and optical properties, *J. Geophys. Res.*, *107*(D21), 4569, doi:10.1029/2001JD001106.

Gayet, J.-F., F. Auriol, A. Minikin, J. Ström, M. Seifert, R. Krejci, A. Petzol, G. Febvre, and U. Schumann (2002b), Quantitative measurement of the microphysical and optical properties of cirrus clouds with four different in situ probes: Evidence of small crystals, *Geophys. Res. Lett.*, *29*(24), 2230, doi:10.1029/2001GL014342.

Gayet, J.-F., V. Shcherbakov, H. Mannstein, A. Minikin, U. Schumann, J. Ström, A. Petzold, J. Ovarlez, and F. Immler (2006), Microphysical and optical properties of midlatitudes cirrus clouds observed in the southern hemisphere during INCA, *Quart. J. R. Meteorol. Soc., Part B*, *132*, 2719–2748.

Gayet, J.-F., R. Treffeisen, A. Helbig, J. Bareiss, A. Matsuki, A. Herber, and A. Schwarzenboeck (2009), On the onset of the ice phase in boundary layer Arctic clouds, *J. Geophys. Res.*, *114*, D19201, doi:10.1029/2008JD011348.

Gerber, H., Y. Takano, T. J. Garrett, and P. V. Hobbs (2000), Nephelometer measurements of the asymmetry parameter, volume extinction coefficient, and backscatter ratio in arctic clouds, *J. Atmos. Sci.*, *57*, 3021–3034, doi:10.1175/1520-0469(2000)057<3021:NMOTAP>2.0.CO;2.

Heymsfield, A. J. (2007), On measurements of small ice particles in clouds, *Geophys. Res. Lett.*, *34*, L23812, doi:10.1029/2007GL030951.

Heymsfield, A. J., D. Winker, and G. J. van Zadelhoff (2005), Extinction–ice water content–effective radius algorithms for CALIPSO, *Geophys. Res. Lett.*, *32*, L10807, doi:10.1029/2005GL022742.

Hlavka, D. L., S. P. Palm, W. D. Hart, J. D. Spinhirne, M. J. McGill, and E. J. Welton (2005), Aerosol and cloud optical depth from GLAS: Results and verification for an October 2003 California fire smoke case, *Geophys. Res. Lett.*, *32*, L22S07, doi:10.1029/2005GL023413.

Hu, Y., et al. (2007), The depolarization–attenuated backscatter relation: CALIPSO lidar measurements vs. theory, *Opt. Express*, *15*, 5327–5332, doi:10.1364/OE.15.005327.

Hunt, W. H., D. M. Winker, M. A. Vaughan, K. A. Powell, P. L. Lucker, and C. Weimer (2009), CALIPSO lidar description and performance assessment, *J. Atmos. Oceanic Technol.*, *26*, 1214–1228, doi:10.1175/2009JTECHA1223.1.

Josset, D., J. Pelon, A. Protat, and C. Flamant (2008), A new approach to determine aerosol optical depth from combined CALIPSO and CloudSat ocean surface echoes, *Geophys. Res. Lett.*, *35*, L10805, doi:10.1029/2008GL033442.

Korolev, A. V., and G. A. Isaac (2005), Shattering during sampling by OAPs and HVPS. Part I: Snow particles, *J. Atmos. Oceanic Technol.*, *22*, 528–543, doi:10.1175/JTECH1720.1.

Lawson, R. P., and B. A. Baker (2006), Improvement in determination of ice water content from two-dimensional particle imagery. Part II: Applications to collected data, *J. Appl. Meteorol. Climatol.*, *45*, 1291–1303, doi:10.1175/JAM2399.1.

Lawson, R. P., B. A. Baker, and C. G. Schmitt (2001), An overview of microphysical properties of Arctic clouds observed in May and July 1998 during FIRE ACE, *J. Geophys. Res.*, *106*(D14), 14,989–15,014, doi:10.1029/2000JD900789.

Lefèvre, R. (2007), *Physique de la mesure de la sonde CPI pour la mesure des propriétés des cristaux de glace. Application aux observations réalisées durant la campagne ASTAR 2004*, 186 pp., Univ. Blaise Pascal, Aubière, France.

Liou, K. N. (1986), Influence of cirrus clouds on weather and climate processes: A global perspective, *Mon. Weather Rev.*, *114*, 1167–1199, doi:10.1175/1520-0493(1986)114<1167:IOCCOW>2.0.CO;2.

Liou, K. N., and Y. Takano (1994), Light scattering by nonspherical particles: Remote sensing and climatic implications, *Atmos. Res.*, *31*, 271–298, doi:10.1016/0169-8095(94)90004-3.

McFarquhar, G., G. Zhang, M. R. Poellot, G. L. Kok, R. McCoy, T. Tooman, A. Fridlind, and A. Heymsfield (2007), Ice properties of single-layer stratocumulus during the mixed-phase arctic cloud experiment: 1. Observations, *J. Geophys. Res.*, *112*, D24201, doi:10.1029/2007JD008633.

McGill, M. J., M. A. Vaughan, C. R. Trepte, W. D. Hart, D. L. Hlavka, D. M. Winker, and R. Kuehn (2007), Airborne validation of spatial properties measured by the CALIPSO lidar, *J. Geophys. Res.*, *112*, D20201, doi:10.1029/2007JD008768.

Noel, V., and H. Chepfer (2004), Study of ice crystal orientation in cirrus clouds based on satellite polarized radiance measurements, *J. Atmos. Sci.*, *61*, 2073–2081, doi:10.1175/1520-0469(2004)061<2073:SOICOI>2.0.CO;2.

Noel, V., and K. Sassen (2005), Study of planar ice crystal orientations in ice clouds from scanning polarization lidar observations, *J. Appl. Meteorol.*, *44*, 653–664, doi:10.1175/JAM2223.1.

Noel, V., D. M. Winker, T. J. Garrett, and M. McGill (2007), Extinction coefficients retrieved in deep tropical ice clouds from lidar observations using a CALIPSO-like algorithm compared to in situ measurements from the cloud integrating nephelometer during CRYSTAL-FACE, *Atmos. Chem. Phys.*, *7*, 1415–1422.

Pelon, J., P. H. Flamant, and M. Meissonnier (1990), The French airborne backscatter lidar Leandre: I. Conception and operation, in *Proceedings of the 15th International Laser Radar Conference, Tomsk, USSR*, edited by V. E. Zuev, pp. 36–39, Inst. of Atmos. Opt., Tomsk, Russia.

Platt, C. M. R. (1979), Remote sounding of high clouds. I: Calculation of visible and infrared optical properties from lidar and radiometer measurements, *J. Appl. Meteorol.*, *18*, 1130–1143, doi:10.1175/1520-0450(1979)018<1130:RSOHCI>2.0.CO;2.

Powell, K. A., M. A. Vaughan, R. Kuehn, W. H. Hunt, and K.-P. Lee (2008), Revised calibration strategy for the CALIOP 532-nm channel. Part II: Daytime, paper presented at 24th International Laser Radar Conference, Lockheed Martin, Boulder, Colo., 23–26 June.

Protat, A., et al. (2004), Le projet RALI: Combinaison d'un radar nuage et d'un lidar pour l'étude des nuages faiblement précipitants, *Meteorologie*, *47*, 23–33.

Protat, A., D. Bouniol, J. Delanoë, P. T. May, A. Plana-Fattori, A. Hasson, E. O'Connor, U. Görsdorf, and A. J. Heymsfield (2009), Assessment of CloudSat reflectivity measurements and ice cloud properties using ground-based and airborne cloud radar observations, *J. Atmos. Oceanic Technol.*, *26*, 1717–1741, doi:10.1175/2009JTECHA1246.1.

Sassen, K. (1980), Remote sensing of planar ice crystal fall attitudes, *J. Meteorol. Soc. Jpn.*, *58*, 422–429.

Sassen, K., and J. M. Comstock (2001), A midlatitude cirrus cloud climatology from the facility for atmospheric remote sensing. Part III: Radiative properties, *J. Atmos. Sci.*, *58*, 2113–2127, doi:10.1175/1520-0469(2001)058<2113:AMCCCF>2.0.CO;2.

Shcherbakov, V., J-F. Gayet, O. Jourdan, J. Ström and A. Minikin (2006), Light scattering by single ice crystals of cirrus clouds. *Geophys. Res. Lett.*, *33*, L15809, doi:10.1029/2006GL026055.

Stephens, G. L., et al. (2002), The CloudSat mission and the A-Train: A new dimension of space-based observations of clouds and precipitation, *Bull. Am. Meteorol. Soc.*, *83*, 1771–1790, doi:10.1175/BAMS-83-12-1771.

Stratton Park Engineering Company (2005), *CPIview: CPI Data Processing Software*, manual, SPEC Inc., Boulder, Colo. (Available at http://www.specinc.com/publications/CPIview_Manual.pdf)

Vaughan, M., S. Young, D. Winker, K. Powell, A. Omar, Z. Liu, Y. Hu, and C. Hostetler (2004), Fully automated analysis of space-based lidar data: An overview of the CALIPSO retrieval algorithms and data products, *Proc. SPIE*, *5575*, 1177–1180.

Vaughan, M. A., K. A. Powell, D. M. Winker, C. A. Hostetler, R. E. Kuehn, W. H. Hunt, B. J. Getzewich, S. A. Young, Z. Liu, and M. J. McGill (2009), Fully automated detection of cloud and aerosol layers in the CALIPSO lidar measurements, *J. Atmos. Ocean. Technol.*, *26*(10), 2034–2050, doi:10.1175/2009JTECHA1228.1.

Wendisch, M., D. Müller, D. Schell, and J. Heintzenberg (2001), An airborne spectral albedometer with active horizontal stabilization, *J. Atmos. Oceanic Technol.*, *18*, 1856–1866, doi:10.1175/1520-0426(2001)018<1856:AASAWA>2.0.CO;2.

Winker, D. M., J. Pelon, and M. P. McCormick (2003), The CALIPSO mission: Spaceborne lidar for observation of aerosols and clouds, status and performance, *Proc. SPIE*, *4893*, 1–11.

Winker, D. M., M. A. Vaughan, A. H. Omar, Y. Hu, K. A. Powell, Z. Liu, W. H. Hunt, and S. A. Young (2009), Overview of the CALIPSO mission and CALIOP data processing algorithms, *J. Atmos. Oceanic Technol.*, *26*, 2310–2323, doi:10.1175/2009JTECHA1281.1.

Wylie, D. P., W. P. Menzel, H. M. Woolf, and K. I. Strabala (1994), Four years of global cirrus cloud statistics using HIRS, *J. Clim.*, *7*, 1972–1986, doi:10.1175/1520-0442(1994)007<1972:FYOGCC>2.0.CO;2.

Young, S. A., and M. A. Vaughan (2009), The retrieval of profiles of particulate extinction from Cloud Aerosol Lidar Infrared Pathfinder Satellite Observations (CALIPSO) data: Algorithm description, *J. Atmos. Oceanic Technol.*, *26*, 1105–1119, doi:10.1175/2008JTECHA1221.1.

A. Garnier, D. Josset, and J. Pelon, Laboratoire Atmosphères, Milieux, Observations Spatiales, UMR 8190, Université Pierre et Marie Curie, CNRS, 4 pl. Jussieu, F-75005 Paris, France.

J.-F. Gayet, G. Mioche, and A. Schwarzenboeck, Laboratoire de Météorologie Physique, UMR 6016, Université Blaise Pascal, CNRS, 24 av. des Landais, F-63177 Aubière, France. (j.f.gayet@opgc.univ-bpclermont.fr)

A. Minikin, Institut für Physik der Atmosphäre, Deutsches Zentrum für Luft- und Raumfahrt, Oberpfaffenhofen, Postfach 1116, D-82230 Wessling, Germany.